Au36(SePh)24 Nanomolecules: Synthesis, Optical Spectroscopy and Theoretical Analysis

Journal:	*Physical Chemistry Chemical Physics*
Manuscript ID	CP-ART-03-2018-001564.R1
Article Type:	Paper
Date Submitted by the Author:	12-Apr-2018
Complete List of Authors:	Rambukwella, Milan; University of Mississippi, Chemistry and Biochemistry Chang, Le; Beijing University of Chemical Technology Ravishankar, Anish; University Of Mississippi, Department of Chemistry and Biochemistry Stener, Mauro; Universita di Trieste, Dipartimento di Scienze Chimiche Fortunelli, Alessandro; Consiglio Nazionale delle Ricerche, ICCOM Dass, Amala; University of Mississippi, Chemistry and Biochemistry

Journal Name

ARTICLE

$Au_{36}(SePh)_{24}$ Nanomolecules: Synthesis, Optical Spectroscopy and Theoretical Analysis

Milan Rambukwella,[a] Le Chang,[bcd] Anish Ravishanker,[a] Alessandro Fortunelli,[d] Mauro Stener,[e] Amala Dass[a,*]

Received 00th January 20xx,
Accepted 00th January 20xx

DOI: 10.1039/x0xx00000x

www.rsc.org/

Here, we report the synthesis of selenophenol (HSePh) protected $Au_{36}(SePh)_{24}$ nanomolecules via ligand-exchange reaction of 4-*tert*-butylbenzenethiol (HSPh-*t*Bu) protected $Au_{36}(SPh\text{-}tBu)_{24}$ with selenophenol, and its spectroscopic and theoretical analysis. Matrix assisted laser desorption ionization (MALDI), electrospray ionization (ESI) mass spectrometry and optical characterization confirms the composition of the as synthesized product is predominantly $Au_{36}(SePh)_{24}$ nanomolecules. Size exclusion chromatography (SEC) was employed to isolate the $Au_{36}(SePh)_{24}$ and temperature dependent optical absorption studies and theoretical analysis were performed. Theoretically, an Independent Component Maps of Oscillator Strength (ICM-OS) analysis of simulated spectra shows that the enhancement in absorption intensity in $Au_{36}(SePh)_{24}$ with respect to $Au_{36}(SPh)_{24}$ is to be ascribed to the absence of interference and/or increased long-range coupling between interband metal core and ligand excitations. This work demonstrates and helps to understand effect of Au-Se bridging on properties of gold nanomolecules.

INTRODUCTION

Thiolate protected gold nanomolecules[1, 2] (Au NMs) have been extensively studied due to their stability[3] and availability of different $Au_n(SR)_m$ nanomolecules[4-9] having size-dependent properties as well as potential application in biomedicine,[10-13] and catalysis.[7, 13-16] In terms of synthesis, gold-thiolate NMs are prepared using synthetic protocols such as two-phase Brust method,[17] one-phase method[18] and post-synthetic steps such as core-size conversion reactions(etching)[19-21] and ligand-exchange reactions[22] with physicochemically different ligands.[23] These post-synthetic steps are crucial for the synthesis of new nanomaterials, with different physical and chemical properties, that are otherwise difficult to produce via direct synthesis.

In general, the replacement of S(thiolate) with Se(selenolate) group, does not change the atomic structure, but modifies the properties.[10, 24-31] However, one recent report by Zhu et al. has shown that modification at the gold-ligand bridging can produce physicochemically different structures.[32] In contrast to reported Au-thiolate NMs, this work reported the $Au_{24}(SePh)_{20}$ crystal structure, with a *prolate* Au_8 kernel protected by two trimeric $Au_3(SePh)_4$ and two *pentameric* $Au_5(SePh)_6$ staples. Selenium has similar properties to sulfur, nevertheless forms stronger covalent bond with gold due to closer atomic radii and electronegativity to that of gold. Thus, in contrast to thiolate protected $Au_n(SR)_m$, selenolate protected $Au_n(SeR)_m$ NMs possess characteristic differences in physical, electrochemical properties, with reported enhanced stability.[33] These differences are attributed to Au-Se bond being more covalent in nature compared to Au-S bond. Selenolate-protected Au NMs have not been extensively studied due to lack of developed synthetic and isolation protocols.

Recently, ligand-exchange reactions were effectively employed for the synthesis of selenolate protected Au NMs. Zhu et al. were the first to report the synthesis and isolation of a selenolate protected $Au_{25}(SePh)_{18}$ via ligand-exchange reaction on phenylethanethiol

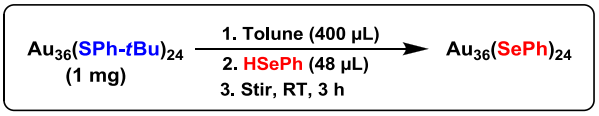

Scheme 1. Synthetic procedure for synthesis of $Au_{36}(SePh)_{24}$ nanomolecules. $Au_{36}(SPh\text{-}tBu)_{24}$, was dissolved in toluene and reacted with excess selenophenol for 3 hours at room temperature.

[a] Department of Chemistry and Biochemistry, University of Mississippi, Oxford, Mississippi, 38677, United States
[b] International Research Center for Soft Matter, Beijing University of Chemical Technology, Beijing 100029, People's Republic of China
[c] State Key Laboratory of Organic–Inorganic Composites, Beijing University of Chemical Technology, Beijing 100029, People's Republic of China
[d] CNR-ICCOM, Consiglio Nazionale delle Ricerche, via Giuseppe Moruzzi 1, 56124, Pisa, Italy
[e] Dipartimento di Scienze Chimiche e Farmaceutiche, Università di Trieste, Trieste I-34127, Italy
Electronic Supplementary Information (ESI) available: MALDI-MS and ESI-MS of $Au_{36}(SePh)_{24}$, Optical spectra, ICM-OS plots of X, Y and Z components. See DOI: 10.1039/x0xx00000x

($HSCH_2CH_2Ph$) protected $Au_{25}(SCH_2CH_2Ph)_{18}$ precursor.[24] Interestingly, the as-synthesized NMs were not soluble in toluene, but were found to be more stable than the precursor $Au_{25}(SCH_2CH_2Ph)_{18}$ NMs. Furthermore these authors were able to modify the reaction conditions and obtain $Au_{18}(SePh)_{14}$ NMs with interesting optical properties.[25] In contrast to Au NMs, Pradeep et al. have reported a stable $Ag_{44}(SePh)_{30}$ having almost identical optical properties that are analogous to thiolate protected $Ag_{44}(SR)_{30}$(ref.[31]).

Herein, we report the synthesis and isolation of selenophenolate(SePh) protected $Au_{36}(SePh)_{24}$ via ligand-exchange reaction with $Au_{36}(SPh\text{-}t\text{Bu})_{24}$ as the precursor. The results show that the core-size of the precursor is retained in the ligand-exchange reaction, while the twenty-four thiolate ligands are completely exchanged to selenophenolates. We find characteristic differences in physical, optical and electrochemical properties of two analogous NMs. Key interesting observation in this present work is how the Au-Se bond affects the optical properties of the NM. Our experimental data and theoretical analysis demonstrate a significant increase in absorption intensity throughout the vis-nearUV region which is interpreted in terms of enhanced coupling (better tuned resonance) between excitations of the metal-core/Au-(seleno)thiolate-shell and the aromatic ligands.

EXPERIMENTAL SECTION

Materials. Hydrogen tetrachloroaurate(III) ($HAuCl_4 .3H_2O$, (Alfa-aesar, 99.9%), sodium borohydride (Acros, 99%), selenophenol (Acros, 99.9%), cesium acetate (Acros, 99%), anhydrous ethyl alcohol (Acros, 99.5%), 4-tert-butylbenzenethiol (Acros, 99%), glutathione (Sigma-Aldrich, 98%), and trans-2-[3[(4-tertbutyl- phenyl)-2-methyl-2-propenylidene]malononitrile (DCTB matrix) (Fluka≥99%) were purchased and used as received. HPLC grade solvents such as tetrahydrofuran, toluene, methanol, butylated hydroxytoluene stabilized tetrahydrofuran (THF-BHT) and acetonitrile were obtained from Fisher Scientific.

Synthesis. Selenophenolate protected $Au_{36}(SePh)_{24}$ NMs were synthesized using two main steps: (i) first step to synthesize $Au_{36}(SPh\text{-}t\text{Bu})_{24}$ precursor and a (ii) second step involving ligand-exchange on $Au_{36}(SPh\text{-}t\text{Bu})_{24}$ with excess selenophenol to obtain $Au_{36}(SePh)_{24}$.

$Au_{36}(SPh\text{-}t\text{Bu})_{24}$, was synthesized according to a previously reported procedure.[34] In a typical synthesis, 200-300 mg of glutathiolate (SG) protected $Au_n(SG)_m$ product was dissolved in 6 mL of distilled water in round bottom flask. To this 2 mL of toluene, 0.3 mL of ethanol and 2 mL of 4-*tert*-butylbenzenethiol was added and etched at 80 °C for about 18 hours. Ethanol was used to facilitate the phase transfer of $Au_n(SG)_m$. After core-size conversion was completed, organic phase was separated and dried to remove remaining solvent, followed by thorough washing. In each of the initial two washing steps, mixture of 10 mL of water and 10 mL of methanol was used to precipitate the product and facilitate the washing step. Finally, the product was extracted with toluene.

Complete selenophenol ligand-exchange on $Au_{36}(SPh\text{-}t\text{Bu})_{24}$ nanomolecules was achieved at room temperature in a single ligand-exchange reaction step. In a typical reaction, $Au_{36}(SPh\text{-}t\text{Bu})_{24}$ was

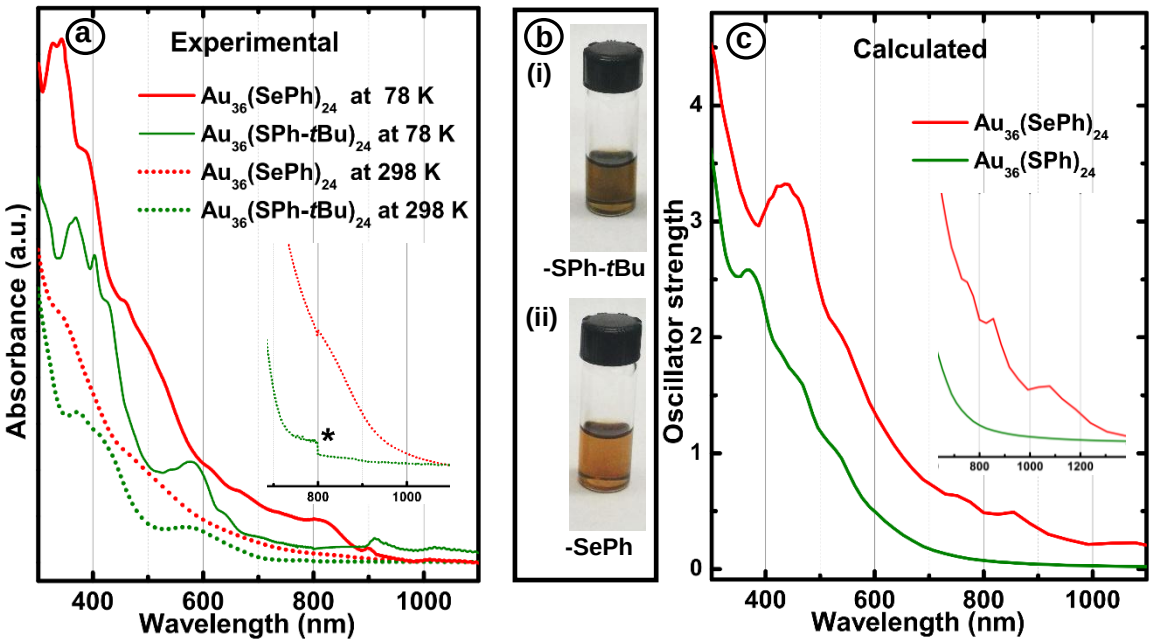

Figure 1. (a) Comparison of the optical spectra of $Au_{36}(SePh)_{24}$ compared with $Au_{36}(SPh\text{-}t\text{Bu})_{24}$ nanomolecules. The inset shows the expansion of the wavelength range, illustrating the difference in onset of absorption of the two nanomolecules. Asterisks shows instrumental artifact due to detector changeover. The red (solid-line) UV-Vis-NIR absorption spectrum of $Au_{36}(SePh)_{24}$ nanomolecules collected at 78 K in methyl-tetrahydrofuran solvent shows characteristic absorption peaks. (b) Visual color comparison of (b.i) green color $Au_{36}(SPh\text{-}t\text{Bu})_{24}$ and (b.ii) reddish-brown $Au_{36}(SePh)_{24}$ NMs. (c) Calculated optical spectra of $Au_{36}(SePh)_{24}$ and $Au_{36}(SPh)_{24}$ nanomolecules. The inset shows the expansion of the wavelength range, illustrating the difference in onset of absorption in the theoretical spectra of the two nanomolecules.

dissolved in toluene (400 μL/ 1 mg) and reacted with excess selenophenol with nanomolecules : selenophenol molar ratio of 1 : 4000 (48 μL / 1 mg) at room temperature for 3 hours. The product was then dried to remove remaining solvent and washed with methanol until a clear supernatant was obtained. The product was extracted with toluene as reddish-brown liquid. The final product was subjected to SEC and $Au_{36}(SePh)_{24}$ was isolated using THF-BHT as the mobile phase. Finally, isolated $Au_{36}(SePh)_{24}$ was washed with methanol several times to remove butylated hydroxytoluene (BHT) and extracted with toluene.

Instrumentation. A Voyager DE PRO mass spectrometer was used to acquire MALDI-TOF mass spectra using DCTB[35] matrix. Compositional analysis was performed with electrospray ionization mass spectra (ESI-MS), collected from Waters Synapt HDMS with THF as the solvent and cesium acetate was added to facilitate ionization via. cesium adduct formation of the analyte.

COMPUTATIONAL APPROACH

1.DFT

The experimental geometry of $Au_{36}(SPh)_{24}$ was taken as a starting point, and fully geometry relaxation was performed using the CP2K package[36] whose DFT algorithms are based on a hybrid Gaussian/Plane-Wave scheme (GPW).[37] Starting from the relaxed geometry of $Au_{36}(SPh)_{24}$, we then replaced S by Se and then fully optimize to obtain the $Au_{36}(SePh)_{24}$ geometry. Pseudopotentials derived by Goedecker, Teter, and Hutter (GTH)[38] were chosen to describe the core electrons of all atoms and DZVP basis sets[39] to represent the DFT Kohn-Sham orbitals. The semi-empirical Grimme-D3 correction[40] was added to the Perdew-Burke-Ernzerhof (PBE)[41] exchange and correlation (xc-) functional to take into account the dispersion interaction between organic ligands. The cutoff for the auxiliary plane-wave representation of the density was 300 Ry.

2.TDDFT

The simulations of the photoabsorption spectra have been performed employing a complex-polarizability TDDFT method. The theory, its implementation and validation against standard TDDFT routines have been reported previously,[42-44] therefore we refer the reader to the original work for further details.

The method is implemented in a local version of the ADF program, and the LB94[45] exchange-correlation (xc-) functional is employed to solve the KS equations. The exchange-correlation kernel is approximated according to the Adiabatic Local Density Approximation (ALDA)[46] in the TDDFT part. A basis set of Slater Type Orbitals (STO) included in the ADF database of triple-zeta polarized (TZP) quality has been employed which has proven to provide fully converged results.[44] A subset of the ADF STO fitting functions is employed to solve the response equations to save computer time without loss of accuracy, as checked in test calculations. Moreover, the Zero Order Regular Approximation (ZORA)[47] is employed to include relativistic effects, which are important for heavy elements such as gold.

To better understand the nature of the optical peaks, we utilize a recently developed original tool – named Independent Component Mapping of Oscillator Strength (ICM-OS) – which follow the lines of and further the connection between absorption and single-particle excitations in the density-matrix form of linear-response self-consistent theory, see Ref.[61] In detail, the z component of the oscillator strength at each given frequency (energy) can be calculated as the imaginary part of the zz diagonal element of the dynamical polarizability tensor as in Ref.[43]:

$$\alpha_{zz}(\omega) = \sum_{i}^{occ}\sum_{a}^{virt} \langle \varphi_i | z | \varphi_a \rangle P_i^a \qquad (1)$$

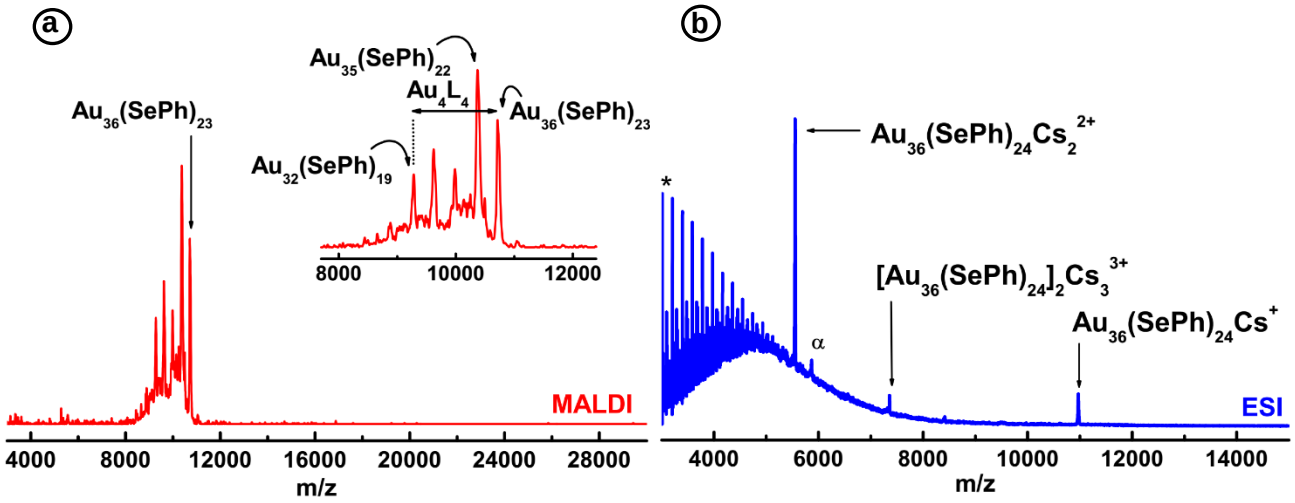

Figure 2. (a) MALDI mass spectra of $Au_{36}(SePh)_{24}$ nanomolecules conforming the purity of the SEC isolated product. (b) ESI mass spectrum of $Au_{36}(SePh)_{24}$ nanomolecules. Spectrum shows 1+, 2+ and dimerized 3+ charge species of $Au_{36}(SePh)_{24}$ nanomolecules. Alpha depicts possible $[Au_{36}(SePh)_{24}Cs_4CH_3COO]^{2+}$ and the asterisk shows $CsCH_3COO$ clusters at mass below 5000 m/z.

where in equation (1) P_i^a is a density matrix element and $\langle\varphi_i|z|\varphi_a\rangle$ is a dipole matrix elements over a pair of occupied/virtual single-particle molecular orbitals (P_i^a in our approach is obtained via Eq. (36) of Ref. [43]). A related previously proposed tool is the Transition Component Mapping (TCM),[48] in which the square of the P_i^a as a function of the one-electron or single-particle energies ε_i and ε_a are plotted with the individual contributions smeared by a Gaussian function to make them visually clearer. However, in TCM the contribution of the dipole matrix elements to the absorption intensity and the sign of the individual single-particle contributions are lost. This is obviated in the ICM-OS method by plotting directly the products $\langle\varphi_i|z|\varphi_a\rangle P_i^a$ as a function of the one-electron or single-particle energies ε_i and ε_a. Contrary to TCM, the resulting plots thus have a positive and negative part, and the total absorption intensity at each given energy is proportional to the integral of the ICM-OS over the (ε_i , ε_a) plane. These plots have been named Independent Component Maps of Oscillator Strength (ICM-OS).[49] They are useful to identify not only the nature of the excited state but also the contribution of the dipole matrix elements to the oscillator strength, especially their relative sign with respect to the corresponding density matrix elements. In detail, ICM-OS consists of a 2D (contours) or 3D (full scale) mapping of the imaginary part of the $\langle\varphi_i|z|\varphi_a\rangle P_i^a$ products, plotted with respect to the energy of the molecular orbitals (occupied on the X axis and virtual on the Y axis) corresponding to the *i* and *a* indexes of expression (1), while the Z axis in the 3D plots corresponds to the ICM-OS values. In both 2D and 3D ICM-OS a colour scale is used to represent different values of the $\langle\varphi_i|z|\varphi_a\rangle P_i^a$ products. Each $\langle\varphi_i|z|\varphi_a\rangle P_i^a$ product corresponds to a point in the XY plane, so a Gaussian function with FWHM=0.12 eV is employed to smooth the point into a surface. ICM-OS plots thus allow one to quantitatively identify enhancing effects in optical phenomena (both traditional plasmonics effects and "rebirth" phenomenon due to proper orbital matching of orbital levels[50]) or quenching effects (such as 5d screening in gold, to be discussed in future work).

RESULTS AND DISCUSSION

Selenium and sulfur belongs to the same group and possess similar properties but, selenium varies from sulfur having closer atomic radius[59] and electronegativity[60] to that of gold (Table 1). Therefore, contributing to a relatively more covalent bond formation with gold.

Table 1. Atomic properties of sulfur, selenium and gold

Property	Sulfur (S)	Selenium (Se)	Gold (Au)
Atomic radius (Å)	1.09	1.22	1.79
Electronegativity (Pauling scale)	2.58	2.55	2.54

In terms of synthesis of $Au_{36}(SePh)_{24}$ NMs, we have observed that the ligand-exchange reaction of $Au_{36}(SPh\text{-}t\text{Bu})_{24}$ with -SePh is significantly rapid. Complete ligand-exchange was observed at room temperature in a single step reaction. The fast reaction rate could be due to less steric crowding and higher affinity[51] of the -SePh ligand compared to -SPh-*t*Bu resulting rapid ligand-exchange. As computed and reported by Pei et al. reaction enthalpy and energetics for the thiolate-selenolate ligand exchange reaction is negative and thermodynamically favorable.[52] As the reaction progress, the green color of the $Au_{36}(SPh\text{-}t\text{Bu})_{24}$ precursor change to reddish-brown color

indicating formation of $Au_{36}(SePh)_{24}$ (fig.1b). The as-synthesized product is stable at ambient conditions. In contrast to $Au_{25}(SePh)_{18}$ reported by Zhu et al.[24] which was toluene insoluble, $Au_{36}(SePh)_{24}$, readily dissolves in toluene. The product was predominately composed of $Au_{36}(SePh)_{24}$ and trace amounts of small clusters such as $Au_{10}(SePh)_{10}$ was found as a by-product of the ligand-exchange reaction. SEC was employed to isolate pure $Au_{36}(SePh)_{24}$ and furthur chareacterization was carried out.

The core structure of the NM is expected to remain intact. The UV-Vis-NIR spectra of reddish-brown color $Au_{36}(SePh)_{24}$ at room temperature (fig.1b(ii). red spectrum) does not show well resolved characteristic absorption peaks compared to the precursor $Au_{36}(SPh\text{-}t\text{Bu})_{24}$. Furthermore, it should be noted that the onset of absorption is lower in energy (~200 nm) compared to $Au_{36}(SPh\text{-}t\text{Bu})_{24}$ nanomolecules (fig.1. inset), indicating a relatively smaller[52] HOMO-LUMO gap as reported by Pei et al. Temperature dependent UV-Vis-NIR absorption spectra were measured in methyl-tetrahydrofuran as a solvent. The spectra obtained at 78 K (Fig. 1. blue spectrum) shows a resolved peak at 345 nm following a shoulder peak at 385 nm and weak absorption bands at 515 and 820 nm. Photoabsorption spectra plotted with respect to the photon energy (Fig.3) show seven distinct peaks. $Au_{36}(SePh)_{24}$ nanomolecules have an extended conjugation due to presence of the aromatic ring adjacent to the Au-Se bridge[53] and the bridging Se results in a bathochromic shift, thereby reducing the band gap energy of the NMs.

Figure 2a. shows MALDI mass spectra of the isolated $Au_{36}(SePh)_{24}$ nanomolecules. Intact 24-ligand was not observed, instead one ligand lost, $Au_{36}(SePh)_{23}$ species was observed which is also commonly observed for thiophenol and tert-butylthiol protected $Au_{36}(SPh)_{24}$(ref.[18, 54]) and $Au_{30}(S\text{-}t\text{Bu})_{18}$(ref.[55]) nanomolecules respectively. Four subsequent fragment-peaks, each corresponding to loss of Au-SePh was observed. MALDI mass spectrum illustrates the highly labile nature of the -SePh ligand at high laser fluence. ESI mass spectrometry is a soft-ionization tool and was used to confirms the composition of the product as $Au_{36}(SePh)_{24}$ due to lack of fragmentation. The $Au_{36}(SePh)_{24}$ nanomolecules were charge neutral and $CsCH_3COO$ was used to impart charge. As a result, molecular peak with one Cs^+ ion adduct, 2+ charge species with two Cs^+ ion adducts was observed at 10,969.7 and 5,551.9 m/z respectively (fig. 2b). Interestingly dimerized 3^+ charged $[[Au_{36}(SePh)_{24}]_2Cs_3]^{3+}$ was observed at 7,357.8 m/z with three Cs^+ ions.

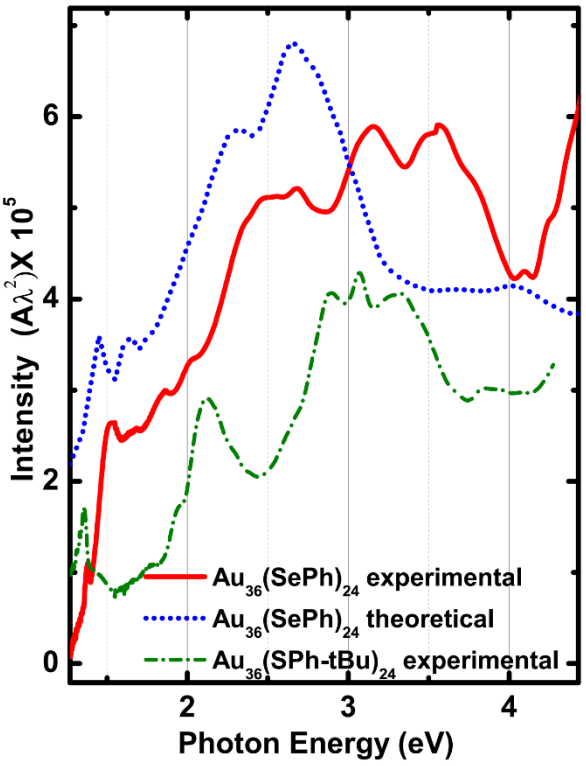

Figure 3. Comparison of experimental and theoretical optical absorption spectra of Au_{36} NMs (multiplied by λ^2).

TDDFT calculation were performed on both $Au_{36}(SePh)_{24}$ and $Au_{36}(SPh)_{24}$ nanomolecules, and the optical spectra are plotted in Figure 1(c) and compared with experimental spectra reported in Figure 1(a) – see the SI for computational details. The comparison between theory and experiment is not perfect: the experimental peak/shoulder at 345/385 nm in the spectrum of $Au_{36}(SePh)_{24}$ should correspond to the peak at 435 nm in the simulated spectrum, but theory fails to reproduce the peak right below 600 nm of $Au_{36}(SPh\text{-}t\text{Bu})_{24}$. Nevertheless, an overall increase in absorption intensity due to replacement by S with Se is well reproduced by theory. The analysis of simulated spectra can thus be focused on 2 regions which exhibit prototypical features: one around 435 nm and one beyond 620 nm, exhibiting distinct differences between $Au_{36}(SePh)_{24}$ and $Au_{36}(SPh)_{24}$.

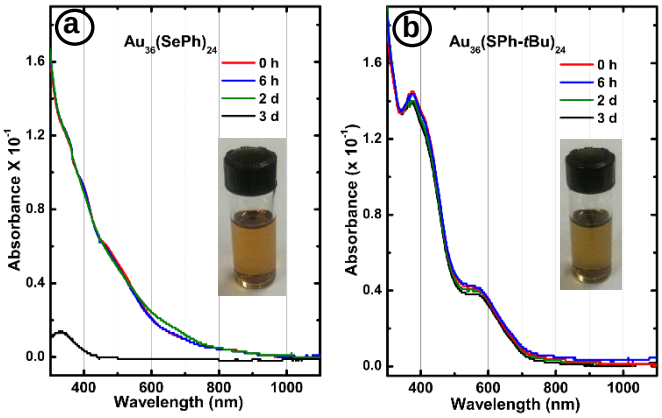

Figure 4. Time dependence absorption spectra of 0.01 mM concentrated (a)$Au_{36}(SePh)_{24}$ and (b) $Au_{36}(SPh\text{-}t\text{Bu})_{24}$ NMs in toluene at 60 °C. Color of the corresponding starting material is shown in each figure.

In the low-energy region, e.g. beyond 620 nm, $Au_{36}(SePh)_{24}$ presents an increase in absorption intensity by a factor ≈2 with respect to $Au_{36}(SPh)_{24}$. This compares reasonably well with the experimental observation of an increase in absorption intensity in the low-energy region beyond 620 nm evident in the spectrum of $Au_{36}(SePh)_{24}$ taken at 78K. It should be recalled that in the experimental compounds the tBu residues in $Au_{36}(SPh\text{-}t\text{Bu})_{24}$ reduce the broadening of the peak at room temperature due to an entropic effect,[56] which could explain part of the discrepancy between theory and experiment.

In the high-energy region, the predicted spectrum of $Au_{36}(SePh)_{24}$ presents a main peak around 435 nm, whereas that of $Au_{36}(SPh)_{24}$ has a peak around 370 nm, blue-shifted with respect to $Au_{36}(SePh)_{24}$. This can be compared with the experimental peak at 345 nm and shoulder at 385 nm for $Au_{36}(SePh)_{24}$ at 78K. Theory does not properly reproduce the position of the experimental peak at 345 nm, but the increase in intensity of the band around 400 nm is reasonably predicted. As the more detailed analysis reported below clarifies, the conjugation between the (metal-selenium) moiety and the π-system of aromatic groups changes decisively the optical response of these systems, making theoretical predictions less precise than in the case of aliphatic residues.

The molecular orbital diagrams of $Au_{36}(SePh)_{24}$ and $Au_{36}(SPh)_{24}$, reported in Fig. S4 in the SI, shows that the energy of the LUMO changes very little (-8.07 eV for $Au_{36}(SePh)_{24}$ and -8.09 eV for $Au_{36}(SPh)_{24}$), whereas the energy of HOMO increases by nearly 0.13 eV for $Au_{36}(SePh)_{24}$ (-9.54 eV compared with -9.67 eV for $Au_{36}(SPh)_{24}$) thus reducing the HOMO-LUMO gap as in the simulations of Pei et al. It is also interesting to note that, in parallel, the Se content in the HOMO increases to 43% for $Au_{36}(SePh)_{24}$ with respect to the S content of 39% in the HOMO of $Au_{36}(SPh)_{24}$ – the Au content in the HOMO is instead similar in $Au_{36}(SePh)_{24}$ (43%) and $Au_{36}(SPh)_{24}$ (43%).

To analyze the main features and better understand the origin of absorption evolution in the high-and low-energy regions, we employ an original analysis of the optical spectrum via Individual Component Maps (ICM-OS) plots (see the SI for more details). 3-dimensional (3D) and 2-dimensional (2D) plots of ICM-OS are reported at 2.0 eV (Fig. 5a) and 2.85 eV (Fig. 5b) in the simulated optical spectra not all Cartesian components are explicitly reported, e.g., the Y component is not reported as its contribution is practically identical to that of the Z component (see Figs. S5, S6 of the SI for partial contributions to the oscillatory strength, while complete ICM-OS plots can be found in Fig. S7, S8).

At low energy (2.0 eV, ~620 nm) the most significant difference in Fig.5a is the broader and more extended range of the positive peaks in the ICM-OS of $Au_{36}(SePh)_{24}$ with respect to $Au_{36}(SPh)_{24}$, which explains the doubled absorption intensity in the optical spectra of $Au_{36}(SePh)_{24}$. In particular, the negative off-diagonal regions in the Z-component $Au_{36}(SPh)_{24}$ ICM-OS nearly disappears in the corresponding ICM-OS of $Au_{36}(SePh)_{24}$, whereas the situation is more complex for the X-component where some compensation/cancellation is still present, however a decrease of negative off-diagonal contributions is anyway apparent. At higher energy (2.85 eV, corresponding to the peak at ~435 nm), the major difference in Fig.5b is again a reduced presence of negative off-diagonal single-electron contributions in $Au_{36}(SePh)_{24}$ with respect to $Au_{36}(SPh)_{24}$, similarly to the analysis at 2.0 eV. This decrease of negative off-diagonal contributions in the ICM-OS plots at both 2.0 and 2.85 eV suggests that the optical response of $Au_{36}(SPh)_{24}$ in the visible is damped by a destructive interference between contribution coming from long-range tails of high-energy excitations, whereas in $Au_{36}(SePh)_{24}$ these contributions interfere mostly constructively with the main peaks, thus increasing oscillator strength and absorption intensity. It should be underlined that, at both low and higher energies, no single, dominant peak is found, and the optical response is spread over a large domain of the of the $(\varepsilon_i, \varepsilon_a)$ plane, with long-range off-diagonal tails especially for $Au_{36}(SePh)_{24}$. This is specifically related with conjugation effects associated with aromatic residues in the thiolates.[53]

The above analysis is confirmed by an inspection of single-particle contributions to oscillator strength reported in Tables S1 and S2 of the SI. At low energy, only a few contributions make up 70% of the oscillator strength of $Au_{36}(SPh)_{24}$, whereas six-times as much contributions make up 70% for $Au_{36}(SePh)_{24}$ (Table S1). Moreover, although only one negative contribution appears for $Au_{36}(SPh)_{24}$, this transition is the second largest in absolute value and represents 9.2% of the total oscillator strength, whereas there are many positive contributions (0.25%-1%) for $Au_{36}(SePh)_{24}$, in keeping with what derived from the ICM-OS plots. At high energy, $Au_{36}(SePh)_{24}$ exhibits twice as many contributions making up 50% of the total oscillator strength as compared with $Au_{36}(SPh)_{24}$, and extended long-range tails with individual contributions of 0.17%-1.0% as in the low-energy case (Table S2).

Finally, concerning thermodynamic quantities, it has been reported in the literature that changing the ligand from thiolate to selenolate has an effect on stability of gold nanomolecules.[24, 28, 33] Negishi et al. reported an interesting in-depth study of ligand induced stability selenolate versus thiolate protected Au_{25} nanomolecules.[33] They found that $[Au_{25}(SeC_8H_{17})_{18}]^-$ was more stable against degradation in solution compared to $[Au_{25}(SC_8H_{17})_{18}]^-$ but results in reduced stability in reactions involving intramolecular dissociation of ligands. Also recently we have observed that, $Au_{36}(SPh)_{24}$ have low stability compared to $Au_{36}(SPh\text{-}t\text{Bu})_{24}$.(ref[57]) To investigates relative stability of the $Au_{36}(SePh)_{24}$ nanomolecules we compared the degradation of $Au_{36}(SePh)_{24}$ against $Au_{36}(SPh\text{-}t\text{Bu})_{24}$ in solution. In brief, 0.01 mM concentration solution of each NM was prepared in toluene and was continuously stirred in an oil bath at 60 °C. Aliquots were taken out at time intervals and UV-vis-NIR spectra of each aliquot was measured (Fig 4). Optical spectra of $Au_{36}(SePh)_{24}$ gradually changes over time and analyte decomposed after 3 days at 60 °C where, $Au_{36}(SPh\text{-}t\text{Bu})_{24}$ showed minimal change in optical absorption spectra. Surprisingly, the results indicate that $Au_{36}(SePh)_{24}$ is not as stable as the $Au_{36}(SPh\text{-}t\text{Bu})_{24}$ in solution. This is opposed to what is reported by Negishi et al. where relatively stable Au_{25} selenolate-protected NMs[33] were reported in contrast to analogous thiolate-protected Au_{25}.

In our early work we have demonstrated that $Au_{38}(SPh)_{24}$ nanomolecules can be prepared starting from phenylethanethiol ($HSCH_2CH_2Ph$) protected $Au_{38}(SCH_2CH_2Ph)_{24}$ nanomolecules via carefully controlled ligand exchange reaction.[58] In a similar fashion, we believe $Au_{38}(SePh)_{24}$ nanomolecules can be synthesized via ligand-exchange reaction of $Au_{38}(SCH_2CH_2Ph)_{24}$ nanomolecules with selenophenol.

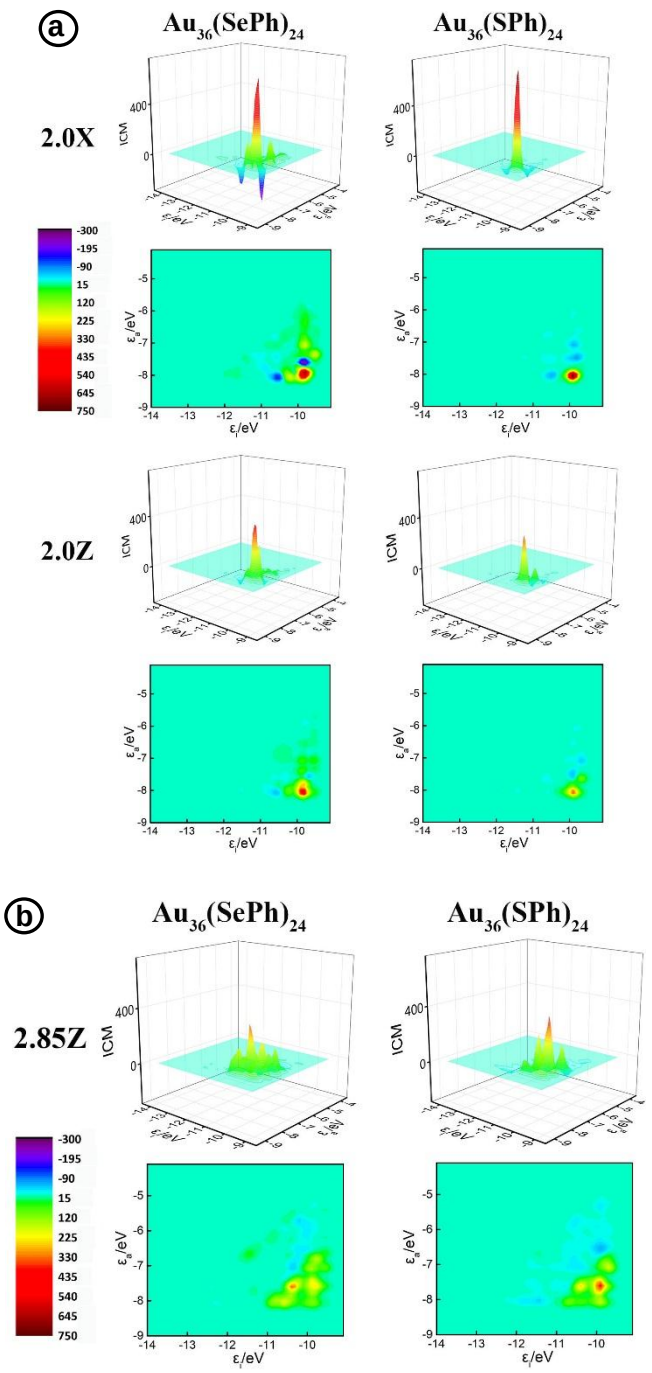

Figure 5. 3D and 2D ICM-OS plots for $Au_{36}(SePh)_{24}$ and $Au_{36}(SPh)_{24}$ nanoclusters. (a) X and Z components at 2.0 eV; (b) X component at 2.85 eV.

CONCLUSIONS

The results here reported demonstrate that $Au_{36}(SePh)_{24}$ can be synthesized via ligand-exchange reaction of $Au_{36}(SPh\text{-}tBu)_{24}$ with selenophenol. The as synthesized $Au_{36}(SePh)_{24}$ shows poorer stability against thermal degradation in toluene solution. Theoretical simulations predict an increase in oscillator strength in both low-energy and high-energy regions in the optical spectrum of $Au_{36}(SePh)_{24}$ compared with $Au_{36}(SPh)_{24}$, in reasonable agreement with experiment. An increase in the energy and in the Se content in the HOMO are found in the electronic structure of $Au_{36}(SePh)_{24}$. This is rationalized and interpreted via an original analysis of the optical response of these complex systems, i.e., the Independent Component Maps of Oscillator Strength (ICM-OS) plots, which shows that the absence of interference and/or increased contribution of long-range single-particle off-diagonal terms are the reasons of the enhancement in absorption intensity in the optical spectra of $Au_{36}(SePh)_{24}$ with respect to $Au_{36}(SPh)_{24}$.

CONFLICTS OF INTEREST

There are no conflicts to declare.

ACKNOWLEDGMENTS

We thank NSF-CHE-1255519 research carrier grant for supporting the work done by M.R. and A.D. LC gratefully acknowledges financial support from the Chinese Scholarship Council. Computational support from the CINECA Supercomputing Centre within the ISCRA Program is gratefully acknowledged.

REFERENCES

1. T. Tsukuda and H. Häkkinen, *Protected Metal Clusters;From Fundamentals to Applications*, Elsevier, Amsterdam, 2015.
2. R. L. Whetten, J. T. Khoury, M. M. Alvarez, S. Murthy, I. Vezmar, Z. L. Wang, P. W. Stephens, C. L. Cleveland, W. D. Luedtke and U. Landman, *Adv. Mater.*, 1996, **8**, 428-433.
3. D.-e. Jiang, M. L. Tiago, W. Luo and S. Dai, *J. Am. Chem. Soc.*, 2008, **130**, 2777-2779.
4. C. Kumara, X. Zuo, J. Ilavsky, K. W. Chapman, D. A. Cullen and A. Dass, *J. Am. Chem. Soc.*, 2014, **136**, 7410-7417.
5. H. Qian, M. Zhu, Z. Wu and R. Jin, *Acc. Chem. Res.*, 2012, **45**, 1470-1479.
6. J.-i. Nishigaki, R. Tsunoyama, H. Tsunoyama, N. Ichikuni, S. Yamazoe, Y. Negishi, M. Ito, T. Matsuo, K. Tamao and T. Tsukuda, *J. Am. Chem. Soc.*, 2012, **134**, 14295-14297.
7. M.-C. Daniel and D. Astruc, *Chem. Rev.*, 2004, **104**, 293-346.
8. Y. Negishi, K. Nobusada and T. Tsukuda, *J. Am. Chem. Soc.*, 2005, **127**, 5261-5270.
9. A. Dass, D. Lee and F. Maran, *Chem.Electro.Chem.*, 2016, **3**, 1191-1192.
10. T. Li, F. Li, W. Xiang, Y. Yi, Y. Chen, L. Cheng, Z. Liu and H. Xu, *ACS Applied Materials & Interfaces*, 2016, **8**, 22106-22112.
11. K. Saha, S. S. Agasti, C. Kim, X. Li and V. M. Rotello, *Chem. Rev.*, 2012, **112**, 2739-2779.
12. A. S. Thakor, J. Jokerst, C. Zavaleta, T. F. Massoud and S. S. Gambhir, *Nano Lett.*, 2011, **11**, 4029-4036.
13. K. Kwak, S. S. Kumar, K. Pyo and D. Lee, *ACS Nano*, 2014, **8**, 671-679.
14. H. Qian, D.-e. Jiang, G. Li, C. Gayathri, A. Das, R. R. Gil and R. Jin, *J. Am. Chem. Soc.*, 2012, **134**, 16159-16162.
15. S. Yamazoe, K. Koyasu and T. Tsukuda, *Acc. Chem. Res.*, 2014, **47**, 816-824.
16. G. Li and R. Jin, *Acc. Chem. Res.*, 2013, **46**, 1749-1758.
17. M. Brust, M. Walker, D. Bethell, D. J. Schiffrin and R. Whyman, *J. Chem. Soc., Chem. Commun.*, 1994, **0**, 801-802.
18. P. R. Nimmala and A. Dass, *J. Am. Chem. Soc.*, 2011, **133**, 9175-9177.
19. T. G. Schaaff and R. L. Whetten, *J. Phys. Chem. B*, 1999, **103**, 9394-9396.
20. R. Jin, H. Qian, Z. Wu, Y. Zhu, M. Zhu, A. Mohanty and N. Garg, *J. Phys. Chem. Lett.*, 2010, **1**, 2903-2910.
21. P. R. Nimmala and A. Dass, *J. Am. Chem. Soc.*, 2014, **136**, 17016-17023.
22. A. Das, C. Liu, C. Zeng, G. Li, T. Li, N. L. Rosi and R. Jin, *J. Phys. Chem. A*, 2014, **118**, 8264-8269.
23. J. Jung, S. Kang and Y.-K. Han, *Nanoscale*, 2012, **4**, 4206-4210.
24. X. Meng, Q. Xu, S. Wang and M. Zhu, *Nanoscale*, 2012, **4**, 4161-4165.
25. Q. Xu, S. Wang, Z. Liu, G. Xu, X. Meng and M. Zhu, *Nanoscale*, 2013, **5**, 1176-1182.
26. Y. Negishi, W. Kurashige and U. Kamimura, *Langmuir*, 2011, **27**, 12289-12292.
27. M. Brust, N. Stuhr-Hansen, K. Nørgaard, J. B. Christensen, L. K. Nielsen and T. Bjørnholm, *Nano Lett.*, 2001, **1**, 189-191.
28. C. K. Yee, A. Ulman, J. D. Ruiz, A. Parikh, H. White and M. Rafailovich, *Langmuir*, 2003, **19**, 9450-9458.
29. D. M. Chevrier, X. Meng, Q. Tang, D.-e. Jiang, M. Zhu, A. Chatt and P. Zhang, *J. Phys. Chem. C*, 2014, **118**, 21730-21737.
30. W. Kurashige, S. Yamazoe, K. Kanehira, T. Tsukuda and Y. Negishi, *J. Phys. Chem. Lett.*, 2013, **4**, 3181-3185.

31. I. Chakraborty, W. Kurashige, K. Kanehira, L. Gell, H. Häkkinen, Y. Negishi and T. Pradeep, *J. Phys. Chem. Lett.*, 2013, **4**, 3351-3355.
32. Y. Song, S. Wang, J. Zhang, X. Kang, S. Chen, P. Li, H. Sheng and M. Zhu, *J. Am. Chem. Soc.*, 2014, **136**, 2963-2965.
33. W. Kurashige, M. Yamaguchi, K. Nobusada and Y. Negishi, *J. Phys. Chem. Lett.*, 2012, **3**, 2649-2652.
34. M. Rambukwella and A. Dass, *Langmuir*, 2017, **33**, 10958-10964.
35. A. Dass, A. Stevenson, G. R. Dubay, J. B. Tracy and R. W. Murray, *J. Am. Chem. Soc.*, 2008, **130**, 5940-5946.
36. J. Hutter, M. Iannuzzi, F. Schiffmann and J. VandeVondele, *Wiley Interdisciplinary Reviews: Computational Molecular Science*, 2014, **4**, 15-25.
37. G. Lippert, J. Hutter and M. Parrinello, *Theor. Chem. Acc.*, 1999, **103**, 124-140.
38. S. Goedecker, M. Teter and J. Hutter, *Phys. Rev. B*, 1996, **54**, 1703-1710.
39. J. VandeVondele and J. Hutter, *J. Chem. Phys.*, 2007, **127**, 114105.
40. S. Grimme, J. Antony, S. Ehrlich and H. Krieg, *J. Chem. Phys.*, 2010, **132**, 154104.
41. J. P. Perdew, K. Burke and M. Ernzerhof, *Phys. Rev. Lett.*, 1996, **77**, 3865-3868.
42. O. Baseggio, M. De Vetta, G. Fronzoni, M. Stener and A. Fortunelli, *Int. J. Quantum Chem*, 2016, **116**, 1603-1611.
43. O. Baseggio, G. Fronzoni and M. Stener, *J. Chem. Phys.*, 2015, **143**, 024106.
44. O. Baseggio, M. De Vetta, G. Fronzoni, M. Stener, L. Sementa, A. Fortunelli and A. Calzolari, *J. Phys. Chem. C*, 2016, **120**, 12773-12782.
45. R. van Leeuwen and E. J. Baerends, *Phys. Rev. A*, 1994, **49**, 2421-2431.
46. E. K. U. Gross and W. Kohn, *Adv. Quantum Chem.*, 1990, **21**, 255-291.
47. E. v. Lenthe, E. J. Baerends and J. G. Snijders, *J. Chem. Phys.*, 1993, **99**, 4597-4610.
48. S. Malola, L. Lehtovaara, J. Enkovaara and H. Häkkinen, *ACS Nano*, 2013, **7**, 10263-10270.
49. S. Theivendran, L. Chang, A. Mukherjee, L. Sementa, M. Stener, A. Fortunelli and A. Dass, *J. Phys. Chem. C*, 2018, **122**, 4524-4531.
50. L. Sementa, G. Barcaro, A. Dass, M. Stener and A. Fortunelli, *Chem. Commun.*, 2015, **51**, 7935-7938.
51. T. M. Carducci, R. E. Blackwell and R. W. Murray, *J. Phys. Chem. Lett.*, 2015, **6**, 1299-1302.
52. J. Zhong, X. Tang, J. Tang, J. Su and Y. Pei, *J. Phys. Chem. C*, 2015, **119**, 9205-9214.
53. L. Sementa, G. Barcaro, O. Baseggio, M. De Vetta, A. Dass, E. Aprà, M. Stener and A. Fortunelli, *J. Phys. Chem. C*, 2017, **121**, 10832-10842.
54. C. Zeng, H. Qian, T. Li, G. Li, N. L. Rosi, B. Yoon, R. N. Barnett, R. L. Whetten, U. Landman and R. Jin, *Angew. Chem. Int. Ed.*, 2012, **51**, 13114-13118.
55. D. Crasto and A. Dass, *J. Phys. Chem. C*, 2013, **117**, 22094-22097.
56. P. R. Nimmala, S. Theivendran, G. Barcaro, L. Sementa, C. Kumara, V. R. Jupally, E. Apra, M. Stener, A. Fortunelli and A. Dass, *J. Phys. Chem. Lett.*, 2015, **6**, 2134-2139.
57. S. Theivendran and A. Dass, *Langmuir*, 2017, **33**, 7446-7451.
58. M. Rambukwella, S. Burrage, M. Neubrander, O. Baseggio, E. Aprà, M. Stener, A. Fortunelli and A. Dass, *J. Phys. Chem. Lett.*, 2017, **8**, 1530-1537.
59. Kenneth Barbalace. Periodic Table of Elements - Sorted by Atomic Radius. EnvironmentalChemistry.com. 1995 - 2017. Accessed on-line: 7/12/2017 https://EnvironmentalChemistry.com/yogi/periodic/atomicradius.html
60. Kenneth Barbalace. Periodic Table of Elements - Sorted by Electronegativity (Pauling). EnvironmentalChemistry.com. 1995 - 2017. Accessed on-line: 7/12/2017 https://EnvironmentalChemistry.com/yogi/periodic/electronegativity.html
61. McWeeny, R.; Methods of Molecular Quantum Mechanics, 2nd ed.; Academic Press; London, **1989**; Chapter 15.

TOC